Structure of the active Fokker-Planck equation

Pedro Herrera and Mario Sandoval*

Department of Physics, Complex Systems, Universidad Autonoma Metropolitana-Iztapalapa, Mexico City 09340, Mexico

(Received 11 March 2023; revised 12 November 2023; accepted 8 January 2024; published 29 January 2024)

This paper solves in one and two dimensions the steady noninteractive active Fokker-Planck (FP) equation and finds that its velocity distribution admits, under limiting cases, a dual behavior. Briefly, when the inertial relaxation time is smaller than the orientation time, the active FP equation admits a bimodal shape, whereas the inverse condition is seen to admit a Gaussian one. Once the velocity distribution functions are available, they are used to find their effect on the system's transport properties, such as its mean-square speed. In the process, a useful mathematical identity for the first kind Bessel function as a sum of bimodal exponential functions is spotted.

DOI: 10.1103/PhysRevE.109.014140

I. INTRODUCTION

The study of active matter with translational inertia (mechanical mass) [1–5] or with rotational inertia (mechanical moment of inertia) [6] or with both inertias [7–15], and even with a generalized rotational inertia (resistance to turn) [16] has been mainly performed by using a Langevin approach; however, a Fokker-Planck (FP) formalism could also be exploited. In this regard, Baskaran and Marchetti [17,18] and Enculescu and Stark [19] formulated an active Fokker-Planck equation including translational and rotational inertia; nevertheless, its steady solution under the assumption that relaxation inertial times (for both translation and rotation) are very small (equivalent to a system under high dissipation) was only proposed. Cavagna *et al.* [16] introduced their spin model with a generalized rotational inertial to understand turning flocks behavior. By assuming that the adjacency matrix among birds is frozen for a given timescale and only within their model, a Boltzmann distribution in velocity and spin space was also proposed. Steffenoni *et al.* [20] applied a multiple scale analysis to the active FP equation with translational inertia and were able to derive a velocity distribution only in the limiting case of high dissipation; that is, the same limit as in Refs. [17–19]. Nevertheless, their scale analysis may shed light on finding a perturbed velocity distribution in the general underdamped case. Vuijk *et al.* [21] posed a FP equation for an active particle with translational inertia and under a magnetic field and found its density distribution in the small-mass limit or equivalently under the assumption of a small translational relaxation time, as in Refs. [17–19,21]. Scholz *et al.* [7] experimentally characterized solid disks of a few centimeters in length with elastic legs and able to propel after they are vertically shaken (called vibrobots). Due to the vibrobot size, translational and rotational inertial effects were detected and it was observed that the vibrobots possessed a bimodal velocity distribution. Additionally, and by mixing information from a Langevin analysis and a Fokker-Planck formalism, Scholz *et al.* [7] found a fitted velocity distribution with translational and rotational inertial effects. Note that Scholz's system satisfies once again the condition of small translational relaxation time. A first attempt to analytically characterize the inertial—in both translation and rotation—active Brownian particle model (IABPs), using a Fokker-Planck formalism, was recently reported by Herrera and Sandoval [22]. They found a perturbation solution for the joint distribution of angle and velocity from which they were able to reproduce previous experimental bimodal behavior for the steady velocity distribution with inertial effects but only in the high dissipation limit. Other recent works using an FP formalism with only translational inertia are Ahmad *et al.* [23], who find the density profile of active Brownian particles under gravity and in the presence of a solid wall, and Mengkai and Zhonghuai [24], who introduced possible useful mathematical techniques to attack the not yet available solution of the FP equation with both translational and rotational inertia.

A result related to the current work and where a dual behavior for the velocity distribution is spotted was recently made by Caprini and Marconi [25]. They dealt with a high-density interacting active system in the inertialess regime (and hence some differences with our current reported physics), and numerically observed that, for small reorientation times, their system's velocity distribution had two peaks (since in the inertialess world an active particle immediately acquires its propulsion speed, and, due to its high rotational noise, the particles making the high density solid practically do not interact, thus being affected just by the propulsion force). On the other hand, for large reorientation times, their velocity distribution showed a Gaussian-like behavior (since at this regime, and due to its slow change in orientation, an active particle making a solid will interact with its neighbors).

As it can be seen, a systematic procedure for solving the steady noninteractive active FP equation with translational inertia (within the IABP model) and for any value of the translational relaxation time, is not yet available. This work will precisely tackle this problem, and on the way it will be

*sem@xanum.uam.mx

discovered that the steady FP solution is actually sensitive to the value of the translational relaxation time, namely, when it is large—compared with the reorientation time—the velocity distribution becomes Gaussian, whereas when it is small (as in all the mentioned works), the distribution becomes bimodal. The latter procedure is carried out in one and two dimensions. Once the velocity PDFs are available, they are used to find possible effects on transport properties such as in the system's mean-square speed. All the new analytical expressions in this work were compared with Langevin dynamics simulations with parameters taken from experiments. It is also worth mentioning that in the process, a mathematical identity for the first-kind Bessel function as a function of bimodal exponential functions was spotted. This identity turned out to be crucial for the analytical expressions found throughout the paper.

For ease of reading, a summary of key ideas from each section of this paper is offered: Section II poses the FP equation for a one-dimensional model, finds a hierarchical equation whose solution solves the steady FP equation, and introduces a perturbation parameter ϵ as a ratio of inertial and reorientation timescales. Section III analytically solves the hierarchical equation (for a one-dimensional model) under two limiting cases ($\epsilon \to 0$ and $\epsilon \to \infty$) and proves the existence of a dual behavior of the steady velocity distribution. The analytical results are verified by comparing them to Langevin simulations. Section IV finds a very useful mathematical identity where the Bessel functions appear and solves the active FP to $O(\epsilon)$. Section V obtains the mean square speed (MSS) for both (Gaussian and bimodal) velocity distributions and establishes that the MSS obtained from a Gaussian distribution is smaller than the one from a bimodal distribution. Section VI solves the FP equation in two dimensions and shows the existence of a volcano-like distribution. Section VII finds the speed distribution in two dimensions by using the discovered mathematical identity thus showing its applicability. Section VIII recovers the classical Maxwell-Boltzmann speed for a passive system from our general expressions, and also shows that the speed distribution for an active system is practically Gaussian. Numerical simulations to validate the analytical expressions are also offered. Finally, Section IX summarizes the current findings.

II. ACTIVE SYSTEM IN ONE DIMENSION

Let us start by considering a one-dimensional dynamics [26,27] (thought as the projection along the x axis of a two-dimensional dynamics[1]) of an active Brownian particle of mass M and zero rotational inertia, described by its translational velocity $v(t)$ and its instantaneous angular position $\varphi(t)$ in the direction of propulsion, namely,

$$M\frac{dv}{dt} = -R_T v + R_T U\cos\varphi + \tilde{f}(t), \tag{1}$$

$$\frac{d\varphi}{dt} = \tilde{g}(t), \tag{2}$$

where R_T is the resistance to translation [thus generalizing it to be either friction (solid-wall) or drag (solid-fluid)], U is the imposed propulsion speed and taken constant for convenience, whereas $\tilde{f}(t)$ and $\tilde{g}(t)$ are zero mean random variables whose correlations are given by $\langle\tilde{f}(t)\tilde{f}(t')\rangle = 2R_T^2 D_T\delta(t-t')$ and $\langle\tilde{g}(t)\tilde{g}(t')\rangle = 2D_R\delta(t-t')$, where D_T and D_R are translational and rotational noise intensities. By using well-known techniques, the corresponding Fokker-Planck equation for the probability distribution function (PDF), $P(v,\varphi,t)$ such that $P(\varphi, v, t) : \mathcal{D}\times[0,T]\to[0,1]$ with $P(\varphi, v=\pm\infty, t)=0$, for Eqs. (1) and (2) can be found expressly as

$$\frac{\partial P}{\partial t} = \frac{1}{\tau_M}\frac{\partial[(v-U\cos\varphi)P]}{\partial v} + \frac{D_T}{\tau_M^2}\frac{\partial^2 P}{\partial v^2} + \frac{1}{\tau_R}\frac{\partial^2 P}{\partial\varphi^2}, \tag{3}$$

where τ_M and τ_R have been defined, respectively, as the inertial and orientational relaxation times ($\tau_M = M/R_T$ and $\tau_R = 1/D_R$). The solution of Eq. (3) is subject to the initial and boundary B conditions, $P(0) = \delta(v-v_0)/2\pi$, $P(\varphi, v, t) = P(\varphi+2\pi, v, t)$, and $B(P, \partial P) = 0$. From now on, we will be interested in solving Eq. (3) in the steady state ($t\to\infty$). Its PDF must satisfy the steady condition $\partial P/\partial t = 0$ and the normalization condition $\int_{-\infty}^{\infty}\int_0^{2\pi} P_s(v,\varphi)dvd\varphi = 1$, where $P_s(v,\varphi) = P(v,\varphi,t\to\infty)$. Taking advantage of the periodicity of the active term, a solution of the following form is sought:

$$P_s(\varphi, v) = \sum_{n=-\infty}^{\infty} p_n(v)e^{in\varphi}, \tag{4}$$

where the hierarchical equation for the p_n functions in its respective Fourier space, $\tilde{p}_n(u) = \int_{-\infty}^{\infty} p_n(v)e^{-iuv}dv$, and after introducing $\tilde{p}_n = q_n(u)\exp(-u^2D_T/2\tau_M)$, to eliminate the translational diffusive term reads

$$u\frac{dq_n}{du} + \frac{iuU}{2}(q_{n-1}+q_{n+1}) + \frac{\tau_M}{\tau_R}n^2 q_n = 0. \tag{5}$$

Notice that Eq. (5) already indicates a coupling effect (due to activity in the system) between functions q_n, q_{n-1}, and q_{n+1}. Before going on, Eq. (5) is written in dimensionless form as

$$\bar{u}\frac{dq_n}{d\bar{u}} + \frac{i\bar{u}U_{th}}{2}(q_{n-1}+q_{n+1}) + \epsilon n^2 q_n = 0, \tag{6}$$

where the dimensionless variables $v_{th} = \sqrt{D_T/\tau_M}$, $U_{th} = U/v_{th}$, and $\bar{u} = uv_{th}$ have been introduced. Here, the parameter $\epsilon = \tau_M/\tau_R$ is also introduced. This parameter will play the role of a perturbation parameter. Note that Eq. (6) represents the core or the main structure of the active FP equation, whose solution will be made in the following section.

III. SOLUTION TO THE STRUCTURE OF THE ACTIVE FOKKER-PLANCK EQUATION

The following sections will prove that the structure of the active Fokker-Planck equation, admits under limiting cases, two different steady PDF behaviors which depend on the magnitude of parameter ϵ. When this parameter is small, $\epsilon \ll 1$, the orientation relaxation time dominates on the inertial time, thus causing a steady bimodal PDF whose peaks are centered around the absolute value of the propulsion speed $(-U, U)$. On the other hand, when $\epsilon \gg 1$, the inertial time

[1]In this sense, a continuous rotation $\in[0, 2\pi]$ of the active particle is preserved.

dominates, thus generating a Gaussian velocity distribution with an effective diffusivity $D_E = D_T + U^2\tau_R/2$. Interestingly, both behaviors can be obtained from the hierarchical system Eq. (6), and a systematic procedure for finding this dual behavior will be built in the next sections.

A. Gaussian behavior ($\epsilon \gg 1$)

Under the limit $\epsilon \gg 1$, one notices that the information beyond $n \geqslant 3$ in Eq. (6) can be neglected in favor to obtain a closed system for the coefficients q_n with $n = 0, \pm 1, \pm 2$. In the same way, the contribution of the first term in Eq. (6) can be neglected with respect to the term with parameter ϵ for $n \geqslant 1$, that is, $\tilde{u}dq_{\pm n}/d\tilde{u} \ll n^2\epsilon q_{\pm n}$ for $n \geqslant 1$. Under these considerations, Eq. (6) for $n = 0, \pm 1, \pm 2$ gives

$$\frac{dq_0}{d\tilde{u}} + \frac{iU_{th}}{2}\mu_1 = 0, \tag{7}$$

$$\frac{iuU}{2}[2q_0 + \mu_2] + \epsilon\mu_1 = 0, \tag{8}$$

$$\frac{iuU}{2}[\mu_1] + 4\epsilon\mu_2 = 0, \tag{9}$$

where function $\mu_n = q_n + q_{-n}$ has been introduced. By introducing Eq. (9) into Eq. (8), the coefficient μ_1 can be represented as a function of q_0. To order $O(1/\epsilon^2)$ this leads to

$$\mu_1 = -\frac{i\bar{u}U_{th}q_0}{\epsilon}\left[\frac{1}{1 + \frac{\bar{u}^2U_{th}^2}{16\epsilon^2}}\right]. \tag{10}$$

On the another hand, by taking the marginal integral with respect to the angular variable φ to Eq. (4), one proves that $P(v) = \int_0^{2\pi} P_s(v,\varphi)d\varphi = 2\pi q_0(v)$, which implies that the velocity distribution will only depend on the coefficient q_0. To explicitly obtain this coefficient, the leading term of Eq. (10) is substituted into Eq. (7) to finally get

$$\frac{dq_0}{d\bar{u}} + \frac{U_{th}^2\bar{u}}{2\epsilon}q_0 = 0, \tag{11}$$

and whose solution is given by $q_0 = A\exp(-U_{th}^2\tilde{u}^2/4\epsilon)$. Returning to the $\tilde{p}$ function (after applying the inverse Fourier transform), and returning to dimensional variables, a Gaussian behavior is finally obtained:

$$P(v) = \sqrt{\frac{\tau_M}{2\pi D_E}}e^{-\frac{v^2\tau_M}{2D_E}}, \tag{12}$$

with $D_E = D_T + U^2\tau_R/2$. This result implies that under the limit $\epsilon \gg 1$, the structure of the steady velocity distribution of an active system is similar to a passive one but with an enhanced effective diffusivity D_E. Notice that the Gaussian distribution given by Eq. (12) may occur under two different scenarios: The first one when τ_M is finite and τ_R tends to zero, and the second one when the τ_R is finite and τ_M tends to ∞. Both scenarios satisfy the condition $\tau_M \gg \tau_R$ or $\epsilon \gg 1$. Physically, the first situation causes a quick change in orientation of the particles, thus preventing them from reaching and maintaining their net velocity around their self-propulsion speed. The second situation generates an opposition of the particles to change their direction (due to their large translational inertia). This opposition generates a mismatch between the particles' velocities and their orientation vector, thus preventing them once again from reaching and maintaining their net velocity around their self-propulsion speed. Both scenarios lead to inertial (in translation) active particles to possess a Gaussian velocity distribution with an enhanced diffusion coefficient D_E.

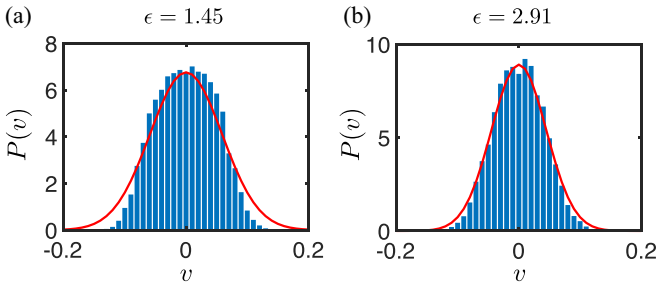

FIG. 1. Gaussian behavior as ϵ increases. The analytical expression, Eq. (12), is represented as a red solid line whereas simulations are indicated as blue bars. In both cases, $M = 4.07 \times 10^{-3}$ kg, $U = 0.0929$ m s^{-1}, $\tau_M = 0.145$ s, $D_T = 7.7 \times 10^{-5}$ m^2 s^{-1}, as dictated by experiments with vibrobots [7]. (a) $\epsilon = 1.45$. (b) $\epsilon = 1.45$. Notice how the simulations tend to a Gaussian shape as the parameter $\epsilon \gg 1$.

Let us now solve Eqs. (1) and (2) using Langevin dynamics simulations—employing a second-order Verlet-type algorithm [9,28]—to validate the predicted Gaussian behavior. For the simulations, available experimental parameters from vibrobots [7] (which are solid disks of order of centimeters with elastic legs and vertically shaken in order to create self-propulsion) will be used. Those parameters are $M = 4.07 \times 10^{-3}$ kg, $U = 0.0929$ m s^{-1}, $\tau_M = 0.145$ s, $D_T = 7.7 \times 10^{-5}$ m^2 s^{-1}. In addition, two different artificial values for its rotational relaxation times, namely, $\tau_R = \{0.01\text{ s}, 0.05\text{ s}\}$ will also be considered. The results are presented in Fig. 1 where the theoretical expression, Eq. (12), is represented as a red solid line, whereas the Langevin simulations are represented in blue bars. Notice that 2000 realizations were employed. Figure 1(a) with $\tau_R = 0.01$ s and hence $\epsilon = 1.45$, indicates that the system has a steady velocity PDF close but not equal to a Gaussian distribution. On the other hand, Fig. 1(b) with $\tau_R = 0.05$ s and hence $\epsilon = 1.91$, possesses an almost perfect Gaussian distribution. Therefore, as the theory predicts, by increasing the parameter ϵ, a Gaussian behavior has to be recovered.

B. Bimodal behavior ($\epsilon \to 0$)

Consider now the limiting case $\epsilon \to 0$ in Eq. (6) and write it in dimensional form expressly as

$$\frac{dq_n}{du} + \frac{iU}{2}(q_{n-1} + q_{n+1}) = 0. \tag{13}$$

This time, the solution of this system is not trivial—as in the Gaussian case—since now the hierarchy given by Eq. (13) is not easy to decouple. To solve it, one can differentiate Eq. (13) with respect to u and introduce in the resulting equation information available from Eq. (13) for the functions $q_{n-1} + q_{n+1}$.

After these steps, a second-order equation for q_n is obtained:

$$\frac{d^2q_n}{du^2} + \frac{U^2}{4}[2q_n + q_{n+2} + q_{n-2}] = 0, \tag{14}$$

where $n \in [-N, 0, N]$ being $N \in \mathbb{Z}^+$, a truncation number. By introducing function $\mu_n = q_n + q_{-n}$, the hierarchical Eq. (14) takes the form

$$\frac{d^2\mu_n}{du^2} + \frac{U^2}{4}[2\mu_n + \mu_{n+2} + \mu_{n-2}] = 0, \tag{15}$$

where, this time, $n \in [0, N]$. In this way, one can see that $\mu_0 = 2q_0$, $\mu_n + \mu_{-n} = 2\mu_n$, and $\mu_{-n} = \mu_n$; thus after this change of variable, only N equations need to be decoupled. Notice that Eq. (15) is not a closed system, thus for this case, the steady velocity PDF contained in q_0 now depends on all the nodes, which implies solving the infinite coupled system given by Eq. (15). To decouple this system, one first rewrites it in matrix form expressly as

$$\ddot{\mathbf{X}} + \frac{U^2}{4}\mathbb{A}\mathbf{X} = 0, \tag{16}$$

where

$$\mathbb{A} = \begin{matrix} 2 & 0 & 1 & 0 & 0 & 0 & 0\dots \\ 0 & 3 & 0 & 1 & 0 & 0 & 0\dots \\ 2 & 0 & 2 & 0 & 1 & 0 & 0\dots \\ 0 & 1 & 0 & 2 & 0 & 1 & 0\dots \\ 0 & 0 & 1 & 0 & 2 & 0 & 1\dots, \\ 0 & 0 & 0 & 1 & 0 & 2 & 0\dots \\ 0 & 0 & 0 & 0 & 1 & 0 & 2\dots \\ \vdots & \vdots & \vdots & \vdots & \vdots & \vdots & \end{matrix} \tag{17}$$

which represents the system's coupling matrix and $\mathbf{X} = (q_0, \mu_1, \mu_2, \dots)^T$ is the solution vector of the system. Since Eq. (16) is an infinite system, it is necessary to truncate it to a certain order N. As shown later, the order in which it should be truncated is linked to the magnitude of the propulsion speed U in the system. Let us express the coupling matrix as $\mathbb{A} = \mathbb{P}\mathbb{D}\mathbb{P}^{-1}$, where $\mathbb{P}$ represents the matrix of eigenfunctions of $\mathbb{A}$, and whose general form is

$$\mathbb{P} = \begin{matrix} a & 0 & b & 0\dots \\ 0 & c & 0 & d\dots \\ e & 0 & f & 0\dots, \\ 0 & g & 0 & h\dots \\ \vdots & \vdots & \vdots & \vdots \end{matrix} \tag{18}$$

with $\mathbb{P}^{-1}$ being its inverse matrix, and $\mathbb{D}$ its diagonal matrix of eigenvalues. Finally, by using linear algebra tools, one can decouple Eq. (16) as

$$\ddot{\mathbf{Z}} + \frac{U^2}{4}\mathbb{D}\mathbf{Z} = 0, \tag{19}$$

where $\mathbf{Z} = \mathbb{P}^{-1}\mathbf{X}$ is now the decoupled vector. Note how system (19) has acquired a simple oscillator form. Thus the solution for q_0 will be

$$q_0 = \sum_{i=0}^{N} c_i Z_i, \tag{20}$$

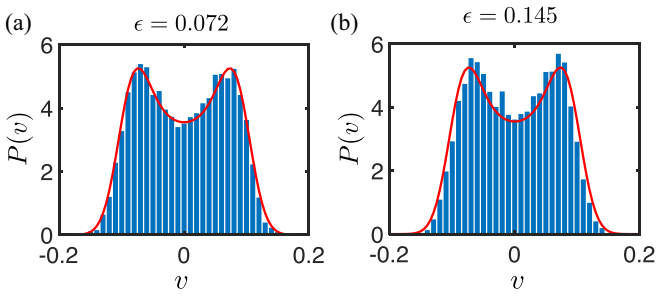

FIG. 2. Bimodal behavior as ϵ decreases. The analytical expression, Eq. (23), is represented in red solid lines, whereas the simulations are in blue bars. For both cases ($\epsilon = 0.072$ and $\epsilon = 0.145$, respectively), only $N = 7$ eigenvalues have been used to plot the analytical bimodal distribution function. An excellent agreement between theory and simulations can be observed.

where c_i are constants, N is the number of functions one wish to consider, and where each function Z_i in Eq. (20) is given by

$$Z_i = A_i e^{\frac{iuU}{2}\sqrt{w_i}} + B_i e^{\frac{-iuU}{2}\sqrt{w_i}}, \tag{21}$$

where w_i is the ith eigenvalue of $\mathbb{A}$. After introducing the appropriate value of each c_i to satisfy the normalization condition, it is possible to verify that q_0 has the following structure:

$$q_0 = \frac{1}{2N}\sum_{i=1}^{N}\left[e^{\frac{iuU}{2}\sqrt{w_i}} + e^{\frac{-iuU}{2}\sqrt{w_i}}\right]. \tag{22}$$

Returning it to $\tilde{p}$ functions, and applying an inverse Fourier transform, one arrives at the steady velocity distribution for an active system in the limit $\epsilon \to 0$, explicitly,

$$P = \sqrt{\frac{\tau_M}{8\pi D_T N^2}}\sum_{i=1}^{N}\left[e^{-\frac{\tau_M\left(v-\frac{U\sqrt{w_i}}{2}\right)^2}{2D_T}} + e^{-\frac{\tau_M\left(v+\frac{U\sqrt{w_i}}{2}\right)^2}{2D_T}}\right], \tag{23}$$

where the exponential functions in the summation represent a typical Gaussian bimodal symmetric distribution. Therefore, Eq. (23) is simply a superposition of N symmetric bimodal functions, whose mean values depend on the eigenvalues of $\mathbb{A}$. Once again, let us validate Eq. (23) by comparing it to Langevin simulations of Eqs. (1) and (2). This system is numerically solved using the same experimental parameters as in Sec. III A. In addition, to satisfy the condition $\epsilon \to 0$, the values $\tau_R = 1$ s implying $\epsilon = 0.145$, and $\tau_R = 2$ s implying $\epsilon = 0.072$ have been artificially chosen. The results for these cases can be seen in Fig. 2, where the theoretical expression, Eq. (23), is represented as red solid lines, whereas Langevin simulations are indicated in blue bars. An excellent agreement between theory and simulations can be appreciated. For both cases, only $N = 7$ eigenvalues have been used. Notice how the peaks of the bimodal distributions are located around the absolute value of the propulsion speed $(-U, U)$. This is due to the fact that under the limit $\tau_M \ll \tau_R$, an active particle is seen to maintain its propulsion around U.

At this stage, we can argue that a bimodal behavior will occur in two different scenarios: the first one when τ_M is finite and τ_R tends to ∞, and the second one when τ_R is finite and τ_M tends to zero. Physically, the first situation involves a very

slow change in the direction of propulsion that causes the particle to maintain its speed around its self-propelled speed. The second situation occurs when the translational inertia is small and does not generate a delay between the velocity vector and the orientation vector. Both situations imply a preference of the active particle to have a velocity magnitude around its self-propelled speed due to the alignment between its velocity vector and its orientation vector, thus generating the observed bimodal behavior. Although it is not shown in the paper, it was observed that the number of necessary eigenvalues to obtain the bimodal distribution (as in Fig. 2) depends on the propulsion value U. In other words, the higher the propulsion, the more eigenvalues will be needed to correctly adjust the theoretical expression, Eq. (23), to the numerical results.

IV. SOLUTION TO THE ACTIVE FOKKER-PLANCK EQUATION FOR $\epsilon << 1$

In Sec. III A, the steady solution to the active Fokker-Planck equation for the case $\epsilon = 0$ has been obtained. As a result, a perfect bimodal behavior profile for the steady velocity PDF has been elucidated. But, What does the $O(\epsilon)$ solution looks like? To answer this, let us nondimensionalize Eq. (3), apply to the resulting equation a Fourier transform, and finally to employ perturbation and characteristic methods. After all these steps, one proves that the dimensional steady velocity distribution solution to Eq. (3), in Fourier space and to $O(\epsilon)$, is given by

$$\tilde{P}(u,\varphi) = \frac{1}{2\pi} e^{-\frac{D_T u^2}{2\tau_M}} e^{-iuU\cos\varphi} H(u,\varphi), \tag{24}$$

with

$$H(u,\varphi) = 1 + \epsilon\left(iuU\cos\varphi - \frac{u^2}{2}U^2\sin^2\varphi\right). \tag{25}$$

This new steady velocity profile in Fourier space is still a function of the angular variable. To remove this angular dependence, one has to apply its angular marginal, $\tilde{P}(u) = \int_0^{2\pi} \tilde{P}(u,\varphi)d\varphi$. The latter step and its velocity distribution form in velocity domain, are not obvious steps. The next section will precisely deal with this.

A. A new mathematical identity

Let us consider the leading-order distribution from Eq. (24),

$$\widetilde{P}(u,\varphi) = \frac{1}{2\pi} e^{-\frac{D_T u^2}{2\tau_M}} e^{-iuU\cos\varphi}, \tag{26}$$

and now let us explicitly obtain its marginal integration with respect to the angle φ. Using the integral definition of the zero-order Bessel function, $J_0(x) = (1/2\pi)\int_0^{2\pi} e^{-ix\cos\varphi}d\varphi$, into Eq. (26); the leading order velocity distribution can be written as

$$\widetilde{P}(u) = e^{-\frac{D_T u^2}{2\tau_M}} J_0(uU). \tag{27}$$

Comparing this expression with the distribution obtained in Sec. III B, specifically with Eq. (23) but in Fourier space, one encounters the following mathematical identity:

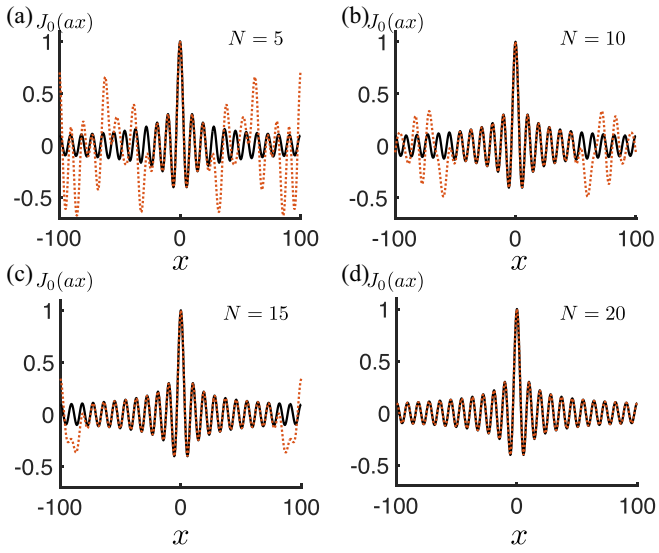

FIG. 3. Comparison between the exact zero-order Bessel function $J_0(ax)$ with $a = 1$ (black solid lines) and Eq. (28), for $N = [5, 10, 15, 20]$ eigenvalues (red dotted lines). Notice how the number of eigenvalues N, used in Eq. (28), generate N peaks in the red dotted functions. Clearly, as $N \to \infty$, the mathematical identity is satisfied.

$$J_0(x) = \frac{1}{2N}\sum_{j=1}^{N}[e^{\frac{-ix}{2}\sqrt{w_j}} + e^{\frac{ix}{2}\sqrt{w_j}}], \quad N \to \infty, \tag{28}$$

where w_i is the ith eigenvalue of matrix $\mathbb{A}$. This time, the Bessel function is expressed as an infinite sum of imaginary exponential functions whose arguments contain the eigenvalues of matrix $\mathbb{A}$. To visualize and corroborate this important result, Eq. (28) is compared with the exact zero-order Bessel function $J_0(x)$. This is shown in Fig. 3 where the exact Bessel function is shown in black solid lines, whereas Eq. (28) for $N = [5, 10, 15, 20]$ eigenvalues is plotted in red dotted lines. Clearly, as the number of eigenvalues increase, the identity perfectly matches the function $J_0(x)$. Notice that the importance of this identity relies on the fact that one can now express a Bessel function as a sum of exponential functions rather than a more complicated classical series form. A formal proof of Eq. (28) is also contained in Appendix A.

Before closing this section, notice that by using Eq. (28) and known properties of Bessel functions, it is possible to express higher-order first-kind Bessel functions as a sum of exponential functions. For example, to get an identity for $J_1(x)$, it is necessary to use the property $J_1(x) = -(d/dx)J_0(x)$ and Eq. (28), which leads to

$$J_1(x) = \frac{1}{2N}\sum_{j=1}^{N}\left(\frac{\sqrt{w_j}}{2i}\right)[e^{\frac{ix}{2}\sqrt{w_j}} - e^{-\frac{ix}{2}\sqrt{w_j}}]. \tag{29}$$

The importance of these identities will be shown in the following sections.

B. Steady velocity distribution to $O(\epsilon)$

By applying the angular marginal integral to Eq. (24), one gets in Fourier space

$$\widetilde{P}(u) = e^{-\frac{D_T u^2}{2\tau_M}}\left[J_0(uU) + \epsilon\frac{uU}{2}J_1(uU)\right]. \tag{30}$$

Taking its inverse Fourier transform, the velocity distribution takes the form

$$P(v) = \frac{1}{2\pi}\left[I_1(v) + \frac{\epsilon U}{2}I_2(v)\right], \tag{31}$$

with

$$I_1(v) = \int_{-\infty}^{\infty} e^{-\frac{D_T u^2}{2\tau_M}} J_0(uU)e^{iuv}du, \tag{32}$$

and

$$I_2(v) = \int_{-\infty}^{\infty} ue^{-\frac{D_T u^2}{2\tau_M}} J_1(uU)e^{iuv}du. \tag{33}$$

As can be seen, Eqs. (31)–(33) indicate that a closed form for the steady velocity seems impossible; however, by taking advantage of Sec. IV A, it is possible to overcome this situation. In this way, one only needs to substitute Eqs. (28) and (29) into the previous integrals to verify that

$$I_1(v) = \frac{1}{2N}\sqrt{\frac{\pi}{a}}\sum_{j=1}^{N}[e^{-\frac{(v-b_j)^2}{4a}} + e^{-\frac{(v+b_j)^2}{4a}}], \tag{34}$$

and

$$I_2(v) = \frac{1}{4Na}\sqrt{\frac{\pi}{a}}\sum_{j=1}^{N}\left(\frac{\sqrt{\omega_j}}{2}\right)[s_j e^{-\frac{s_j^2}{4a}} - h_j e^{-\frac{h_j^2}{4a}}], \tag{35}$$

where $s_j = v + b_j$, $h_j = v - b_j$, $b_j = \frac{U}{2}\sqrt{w_j}$, $a = D_T/2\tau_M$, and i is the imaginary number. With the latter result it is now possible to have a closed steady velocity PDF form summarized by Eq. (31). Let us validate this expression by comparing it to Langevin simulations. To do so, let us take the following available experimental [7] parameters: $M = 1.57 \times 10^{-3}$ kg, $\tau_M = 0.33$ s, $D_T = 2.2 \times 10^{-4}$ m^2 s^{-1}, $\tau_R = 1.69$ s. In addition, four different propulsion speeds $U = (0.087, 0.2, 0.5, 0.8)$ m/s are also considered. Notice that, for this vibrobot, $\epsilon = 0.19$, hence according to our theory ($\epsilon \ll 1$), this vibrobot has to have a bimodal distribution which is experimentally corroborated in Ref. [7]. The results can be visualized in Fig. 4, where the red solid lines represent the theoretical expression, Eq. (31), with $N = 14$ eigenvalues. The yellow dashed lines represent the perfect bimodal, Eq. (23), and the blue bars represent the numerical results. In all cases, the difference between the perfect bimodal, Eq. (23), and the perturbed solution, Eq. (31), can be appreciated. The latter being more accurate—at the extremes and in the middle zone of the PDF—with respect to Langevin simulations. Notice as well, that the peaks in the perturbed solution, become less accurate as the propulsion U grows. This may be overcome if more orders in the perturbed solution are considered.

V. MEAN SQUARE SPEED

What about the ability of Eqs. (12), (23), and (31) to predict the system's mean square speed (MSS)? Using the MSS

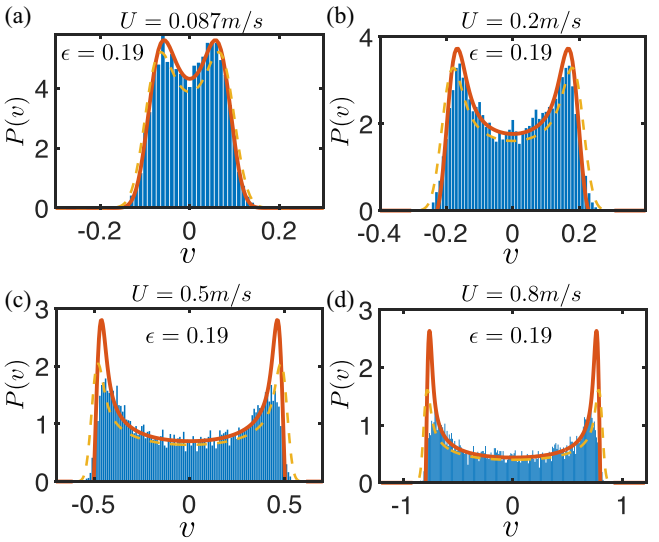

FIG. 4. Theoretical and numerical bimodal distributions for an active system with parameters (taken from previous experimental work): $M = 1.57 \times 10^{-3}$ kg, $\tau_M = 0.33$ s, $D_T = 2.2 \times 10^{-4}$ m^2 s^{-1}, $\tau_R = 1.69$ s; and for different proposed propulsion speeds. (a) $U = 0.087$ m/s, (b) $U = 0.2$ m/s, (c) $U = 0.5$ m/s, and (d) $U = 0.8$ m/s. In all cases, the red solid line represents the theoretical expression, Eq. (31). Yellow dashed line represents the perfect bimodal ($\epsilon \to 0$), Eq. (23); whereas the blue bars represent the numerical results. The numerical results verify how first-order corrections in ϵ improve the adjustment between the theoretical distribution and the numerical simulation at its extremes and at its middle zone; however, as the propulsion increases, a mismatch between the numerical and theoretical maxima starts to appear, see Figs. 4(c) and 4(d). This may be overcome if more eigenvalues are considered. The present figure uses $N = 14$ eigenvalues.

definition

$$\langle v^2\rangle = \int_{-\infty}^{\infty} v^2 P(v)dv, \tag{36}$$

and introducing Eq. (12) into it, one can show that the MSS $\langle v^2\rangle_G$ for active matter with a Gaussian behavior in its velocity distribution is

$$\langle v^2\rangle_G = \frac{D_E}{\tau_M}. \tag{37}$$

The latter expression indicates that under this condition, our active system behaves as a passive one but with an effective diffusivity D_E. For the bimodal case, Eq. (31) is introduced into Eq. (36), and after certain algebraic steps, one can prove that its respective MSS $\langle v^2\rangle_B$ takes the following form:

$$\langle v^2\rangle_B = \frac{1}{N}\sum_{i}^{N}\left[2a + b_i^2 - \frac{\epsilon U}{2}\sqrt{w_i}b_i\right]. \tag{38}$$

Let us rewrite the latter equation by employing summation properties and the following important discovered relation for the eigenvalues w_j of $\mathbb{A}$,

$$\sum_{j=1}^{N} w_j^k = \frac{(2k)!N}{(k!)^2}, \tag{39}$$

where k is any integer. Details on the way this relation is obtained can be seen in Appendix A. Notice that, only after the use of Eq. (39) can one obtain a closed theoretical expression for $\langle v^2\rangle_B$, explicitly,

$$\langle v^2\rangle_B = \left[\frac{D_T}{\tau_M} + \frac{U^2}{2}\left(1 - \frac{\tau_M}{\tau_R}\right)\right]. \tag{40}$$

This expression contains the parameter $\epsilon = \tau_M/\tau_R$ as a correction in the active term, which is due to the presence of translational inertia in the system. Notice that this correction term can be improved if the perturbed solution, Eq. (24), is obtained at higher orders. Let us visualize this by considering the full expression (no approximations applied whatsoever) reported by Sandoval [9] for the MSS of an active Brownian particle with translational inertia and obtained using a Langevin formalism. That formula expressed in current variables reads

$$\langle v^2\rangle = \left[\frac{D_T}{\tau_M} + \frac{U^2}{2(1+\epsilon)}\right]. \tag{41}$$

It is worth noticing that Eq. (41) is valid for any value of ϵ. Hence by applying the limit $\epsilon \ll 1$ to it, and considering that $1/(1+x) = \sum_{k=0}^{\infty}(-1)^k x^k$ for $x \ll 1$, one recovers Eq. (40). This fact corroborates our theoretical procedure. Once the analytical expressions, Eqs. (37) and (40), are available, we proceed to validate them by using Langevin dynamics simulations. Let us reproduce the MSSs for the systems analyzed in Secs. III A and III B. The results as a function of τ_R and U, can be seen in Fig. 5, where the red dots represent the numerical results, while the black dashed lines indicate the theory. Figure 5(a) shows the system's MSS for $\tau_R = \{2, 1, 0.05, 0.025, 0.016\}$ s. The first two cases, $\tau_R = \{2, 1\}$ s or equivalently $\epsilon = \{0.07, 0.14\}$ represent a bimodal behavior, while the rest $\tau_R = \{0.05, 0.025, 0.016\}$ s or equivalently $\epsilon = \{2.91, 5.83, 8.75\}$ represent Gaussian behavior. The other used numerical parameters for the simulations in Fig. 5 are, respectively, the same as in Secs. III A and IV. An excellent agreement between theory and simulations, except for the case $\tau_R = 0.05$ s, can be observed. In the latter case, there is a difference between the numerics and the theoretical expression (37) due to the value of the perturbation parameter, which in this case lies between the transition from a bimodal to a Gaussian distribution. To overcome this, another methodology able to fully solve the active Fokker-Planck equation would be needed. Finally, Fig. 5(b) represents the MSS for the system analyzed in Sec. IV and for different assumed propulsion speeds, namely, $U = [0.087, 0.2, 0.5, 0.8]$ m/s. An excellent agreement between theory and simulations can be appreciated, thus validating Eq. (40).

An important remark from this section is the fact that Eqs. (37) and (40) under their respective limits, satisfy $\langle v^2\rangle_G < \langle v^2\rangle_B$ which may have effects on the information transfer speed in a collection of interacting particles such as in flocks, herds, swarms or schools. Here, information transfer among members of the group may depend on how fast an individual moves; in other words, information transfer may be sensitive to whether the system possesses a Gaussian or a bimodal velocity distribution.

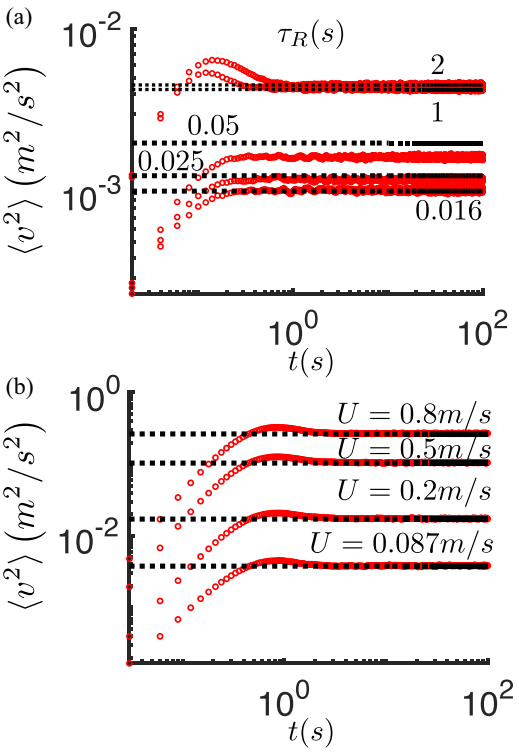

FIG. 5. Theoretical and numerical MSS for an active system as a function of rotational noise and propulsion. (a) MSS for the system analyzed in Sec. III A but for different rotational noises, namely, $\tau_R = \{2, 1, 0.05, 0.025, 0.016\}$ s. (b) MSS for the system analyzed in section (4) but for different propulsion speeds $U = [0.087, 0.2, 0.5, 0.8]$ m/s. In both cases the red dots represent numerical results and the black dashed lines represent theoretical results.

VI. VELOCITY DISTRIBUTION IN TWO DIMENSIONS

So far, the core structure of the active Fokker-Planck equation has been elucidated in a one-dimensional system. Let us then generalize the previous sections to a two-dimensional scenario. For this case, the dynamics of an active Brownian particle with only translational inertia, satisfies the following Langevin dynamics:

$$M\frac{d\mathbf{v}}{dt} = -R_T\mathbf{v} + R_T U\hat{\mathbf{u}} + \tilde{\mathbf{f}}(t), \tag{42}$$

$$\frac{d\varphi}{dt} = \tilde{g}(t), \tag{43}$$

where $\mathbf{v} = (v_x, v_y)$ represents the velocity vector, $\hat{\mathbf{u}} = (\cos\varphi, \sin\varphi)$ is the orientation vector, and $\tilde{\mathbf{f}}(t) = (\tilde{f}_x(t), \tilde{f}_y(t))$ together with $\tilde{g}(t)$ are zero mean random variables whose correlation are given by $\langle \tilde{f}_i(t)\tilde{f}_j(t')\rangle = 2R_T^2 D_T\delta_{ij}\delta(t-t')$ and $\langle \tilde{g}(t)\tilde{g}(t')\rangle = 2D_R\delta(t-t')$.

The respective Fokker-Planck equation for the probability distribution function (PDF), $P(\mathbf{v}, \varphi, t)$, from Eqs. (42) and (43), is given by

$$\frac{\partial P}{\partial t} = \frac{1}{\tau_M}\nabla\cdot[(\mathbf{v} - U\hat{\mathbf{u}})P] + \frac{D_T}{\tau_M^2}\nabla^2 P + \frac{1}{\tau_R}\frac{\partial^2 P}{\partial\varphi^2}, \tag{44}$$

where $\nabla = (\partial_x, \partial_y)$. Its steady solution is sought by nondimensionalizing Eq. (44), applying a double Fourier transform

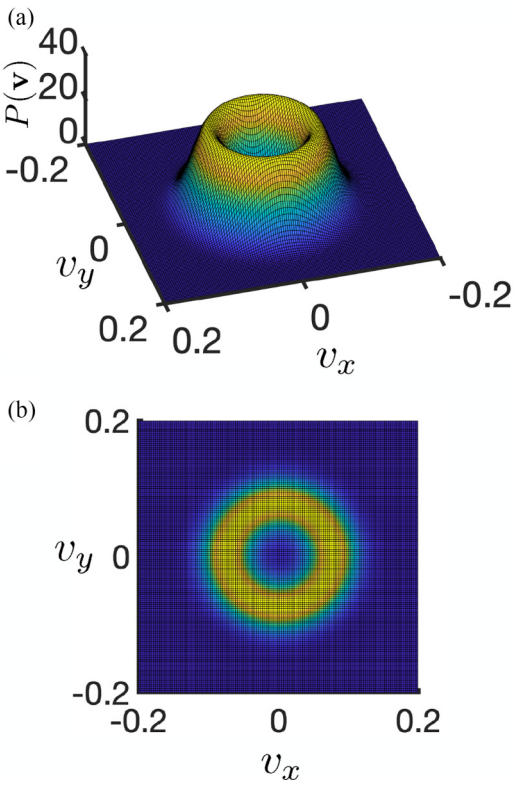

FIG. 6. (a) Velocity distribution $P(\mathbf{v})$, for an active system with parameters (taken from previous experiments) $M = 1.57 \times 10^{-3}$ kg, $\tau_M = 0.33$ s, $D_T = 2.2 \times 10^{-4}$ m^2 s^{-1}, $\tau_R = 1.69$ s, and $U = 0.087$ m/s. This time, a volcano structure has appeared. (b) Projection of $P(\mathbf{v})$ onto the plane v_x-v_y. In both figures, dark colors indicate lower probability, whereas bright colors indicate the opposite.

$[\mathbf{k} = (k_x, k_y)]$ and then using perturbation ($\epsilon = \tau_M/\tau_R \ll 1$) and characteristic methods [22]. After all these steps, the steady velocity PDF in dimensional form becomes

$$\widetilde{P}(\mathbf{k}, \varphi) = e^{-\frac{|\mathbf{k}|^2 D_T}{2\tau_M}} e^{-iU\mathbf{k}\cdot\hat{\mathbf{u}}} \tilde{E}(\mathbf{k}, \varphi), \tag{45}$$

where

$$\tilde{E}(\mathbf{k}, \varphi) = 1 + \epsilon \left\{ iU\mathbf{k}\cdot\hat{\mathbf{u}} - \frac{U^2}{2}\left[\mathbf{k}\cdot\frac{\partial\hat{\mathbf{u}}}{\partial\varphi}\right]^2 \right\}. \tag{46}$$

The latter velocity distribution can also be written in real space, $P(\mathbf{v}, \varphi)$, expressly:

$$P(\mathbf{v}, \varphi) = \frac{\tau_M}{4\pi^2 D_T} e^{-\frac{\tau_M}{2D_T}|\mathbf{v} - U\hat{\mathbf{u}}|^2} E(\mathbf{v}, \varphi), \tag{47}$$

where

$$E = 1 - \epsilon\left(\frac{\tau_M}{D_T}\right)\left\{ U\mathbf{v}\cdot\hat{\mathbf{u}} - \frac{U^2}{2}\left[1 + \frac{\tau_M}{D_T}\left(\mathbf{v}\cdot\frac{\partial\hat{\mathbf{u}}}{\partial\varphi}\right)^2\right]\right\}. \tag{48}$$

However, to obtain its angular marginal, $P(\mathbf{v}) = \int_0^{2\pi} P(\mathbf{v}, \varphi)d\varphi$, a numerical algorithm has to be implemented. After this, one finds that $P(\mathbf{v})$ represents a volcano-shape distribution [Fig. 6(a)] and whose projection on the v_x-v_y plane forms a disk of radius equal to the propulsion speed U. This volcano structure means that the net speed of the system $v^2 = v_x^2 + v_y^2$ has a high probability to be around the propulsion speed U. The latter is shown in Figs. 6(a) and 6(b), where a dark color code is used to represent a lower probability, whereas a bright color code is used to indicate a higher probability.

VII. SPEED DISTRIBUTION IN TWO DIMENSIONS

To obtain the speed distribution, $P_v(v) = 2\pi v P(v)$, where $v^2 = v_x^2 + v_y^2$, it is necessary to find its relation with the velocity distribution, $P(\mathbf{v})$, which implies that a relation between its respective Fourier transform, $\tilde{P}(\mathbf{k})$, and its respective expression as a function of the modulus of the Fourier vector, $\tilde{P}(k)$ exists. In fact, by applying the Fourier transform to Eq. (47), one gets

$$\widetilde{P}(\mathbf{k}) = e^{-\frac{D_T k^2}{2\tau_M}}\left[J_0(Uk) + \epsilon\frac{Uk}{2}J_1(Uk)\right], \tag{49}$$

where $k^2 = k_x^2 + k_y^2$ is the magnitude of vector $\mathbf{k}$. The latter implies that at least to $O(\epsilon)$, $\widetilde{P}(\mathbf{k}) = \widetilde{P}(k)$. Thus, by taking the inverse Fourier transform to $\tilde{P}(\mathbf{k})$, it is possible to verify—after using the change of variables $k_x = k\cos\theta$, $k_y = k\sin\theta$, $v_x = v\cos\phi$, and $v_y = v\sin\phi$—that the relation between the speed distribution $P(v)$ and $\tilde{P}(k)$ is given by the Hankel transform [29]:

$$P(v) = \int_0^\infty k\widetilde{P}(k)J_0(kv)dk. \tag{50}$$

Notice that, by definition, the Hankel transform contains a $J_0(kv)$ function. Henceforth, if one tries to perform this integration in Eq. (49), together with a series representation for the Bessel function, a solution with four indices would appear. The latter fact shows the importance of the identity for $J_0(x)$ given by Eq. (28). After introducing Eq. (49) into Eq. (50), it is possible to rewrite the integral as

$$P(v) = \frac{1}{2\pi}\left[I_1(v) + \epsilon\frac{U}{2}I_2(v)\right], \tag{51}$$

where

$$I_1(v) = \int_0^\infty k e^{-\frac{D_T k^2}{2\tau_M}} J_0(Uk)J_0(kv)dk, \tag{52}$$

and

$$I_2(v) = \int_0^\infty k^2 e^{-\frac{D_T k^2}{2\tau_M}} J_1(Uk)J_0(kv)dk. \tag{53}$$

By using our identity, Eq. (28), the latter integrals can now be calculated. These integrals take the form

$$I_1(v) = \frac{1}{2aN^2}\sum_{j,m=1}^{N}[1 - X_1F(X_1) - X_2F(X_2)], \tag{54}$$

$$I_2(v) = \frac{1}{4aN^2}\sum_{j,m=1}^{N}\sqrt{w_j}\left[\sqrt{\frac{1}{a}}\left(\frac{1}{2} - X_1^2\right)F(X_1) + \frac{b_1}{4a}\right] + \frac{1}{4aN^2}\sum_{j,m=1}^{N}\sqrt{w_j}\left[\sqrt{\frac{1}{a}}\left(\frac{1}{2a} - X_2^2\right)F(X_2) + \frac{b_2}{4a}\right], \tag{55}$$

where $X_1 = b_1/\sqrt{4a}$, $X_2 = b_2/\sqrt{4a}$, $b_1 = q_{jm}/2$, $b_2 = s_{jm}/2$, $q_{jm} = U\sqrt{w_j} + v\sqrt{w_m}$, $s_{jm} = U\sqrt{w_j} - v\sqrt{w_m}$, $a = D_T/2\tau_M$ and where $F(X)$ represents the Dawson function [29]. To conclude, Eq. (51) together with Eqs. (54) and (55), represent the two-dimensional speed distribution for an active Brownian particles of mass M, zero rotational inertia, and under the limit $\epsilon \ll 1$. In the following section, this analytical speed distribution will be studied and plotted under different limits.

VIII. VISUALIZING THE SPEED DISTRIBUTION

Let us now visualize and at the same time corroborate the speed distribution, $P_v(v) = 2\pi P(v)$, [where $P(v)$ is given by Eq. (51)] for three different cases, namely, passive particles ($U = 0$)—for which the classical Maxwell-Boltzmann distribution is expected, an active system with $\epsilon = 0$, and an active system with $\epsilon \ll 1$ but finite.

A. Passive case $U = 0$

Take $U = 0$ in Eq. (51), hence the speed distribution reduces to

$$P(v) = \frac{1}{4a\pi N}\sum_{m=1}^{N}[1 - 2X_1F(X_1)], \tag{56}$$

where in this particular case $X_1 = b_1/\sqrt{4a}$, with $b_1 = v\sqrt{w_m}/2$. Consider now the Dawson function $F(X)$ in its series representation [29],

$$F(x) = -\frac{1}{2}\sum_{k=1}^{\infty}\frac{(-1)^k x^{2k-1}4^k k!}{(2k)!}, \tag{57}$$

and introduce it in Eq. (56). After some manipulation one finds

$$P(v) = \frac{1}{2aN(2\pi)}\left[N + \sum_{k=1}^{\infty}\frac{(-1)^k 4^k k!}{(2k)!(4a)^k}\left(\frac{v^2}{4}\right)^k\sum_{m=1}^{N}w_m^k\right]. \tag{58}$$

Note that the eigenvalues of matrix $\mathbb{A}$ have appeared in the second term of the latter expression. Thus, after using Eq. (39) and some algebra, one finally arrives at

$$P(v) = \frac{1}{2a(2\pi)}e^{-\frac{v^2}{4a}}, \tag{59}$$

which is precisely the classical Maxwell-Boltzmann distribution for passive matter. This result validates the approach taken in this work, since it explicitly shows how Eq. (51) contains under a particular limit, the well-known Maxwell-Boltzmann distribution.

B. Active system, case $\epsilon \to 0$

Let us now consider the leading order of Eq. (51), namely,

$$P(v) = \frac{1}{4a\pi N}\sum_{m=1}^{N}[1 - X_1F(X_1) - X_2F(X_2)], \tag{60}$$

where $X_1 = b_1/\sqrt{4a}$, $X_2 = b_2/\sqrt{4a}$, $b_1 = q_{jm}/2$, $b_2 = s_{jm}/2$, $q_{jm} = U\sqrt{w_j} + v\sqrt{w_m}$, $s_{jm} = U\sqrt{w_j} - v\sqrt{w_m}$, and $a = D_T/2\tau_M$. Using the same series expansion for the Dawson function [Eq. (57)] and the eigenvalues property, Eq. (39), it is possible to verify that the speed distribution, Eq. (60), takes the form

$$P(v) = \frac{1}{4a(2\pi)}\sum_{k=0}^{\infty}\frac{(-1)^k k!}{(4a)^k}\sum_{n=0}^{k}\frac{U^{2(k-n)}v^{2n}}{(n!)^2[(k-n)!]^2}, \tag{61}$$

which can be rewritten, after employing the binomial theorem as well as the property $(\sum_{n=0}^{k}a_n)^2 = \sum_{n=0}^{k}a_n^2 + \sum_{n=0}^{k}\sum_{m\neq n}^{k}a_n a_m$, as

$$P(v) = \frac{1}{2a(2\pi)}e^{-\frac{1}{4a}(U+v)^2} - \frac{1}{4a(2\pi)}\sum_{k=0}^{\infty}\frac{(-1)^k k!}{(4a)^k} \times \sum_{n=0}^{k}\sum_{m\neq n}^{k}\left(\frac{U^{k-n}v^n}{n!(k-n)!}\right)\left(\frac{U^{k-m}v^m}{m!(k-m)!}\right). \tag{62}$$

On the other hand, the series form of a Gaussian distribution is

$$e^{-\frac{(U-v)^2}{4a}} = \sum_{k=0}^{\infty}\frac{(-1)^k(U-v)^{2k}}{(4a)^k k!}. \tag{63}$$

The latter indicates that Eq. (62) is not exactly Gaussian but very close to it, as it can be visualized in Fig. 7, where Eq. (62) is plotted as a red solid line, while a Gaussian distribution, $P(v) = C\exp[(U-v)^2/4a]$, where by normalization, $C^{-1} = 2ae^{-\frac{U^2}{4a}} + \sqrt{\pi a}U[1 + \mathrm{erf}(U/\sqrt{4a})]$ with $a = D_T/2\tau_M$, is plotted as a blue dashed line. The same numerical values as in Sec. IV have been used. Notice that setting $U = 0$ implies that $C^{-1} = 2a$, thus recovering the passive Maxwell-Boltzmann velocity distribution function, Eq. (59).

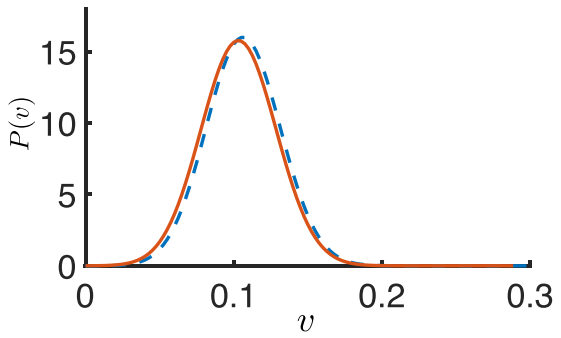

FIG. 7. Speed distribution for a two-dimensional active system in the limit $\epsilon \to 0$. The obtained distribution Eq. (61) is shown in a red solid line; while a perfect Gaussian distribution, Eq. (63), is drawn in a blue dashed line. Note how the speed distribution for an active system under the limit $\epsilon \to 0$ seems to be practically a Gaussian distribution.

C. Active system, cases $\epsilon << 1$

Let us finally visualize Eq. (51) for a finite ϵ. To do so, a comparison between Langevin dynamics and Eq. (51) is carried out. This comparison is shown in Fig. 8(a) where different propulsions, namely, $U = [0, 0.087, 0.15, 0.2]$ m/s are considered and the same parameters from Sec. IV are

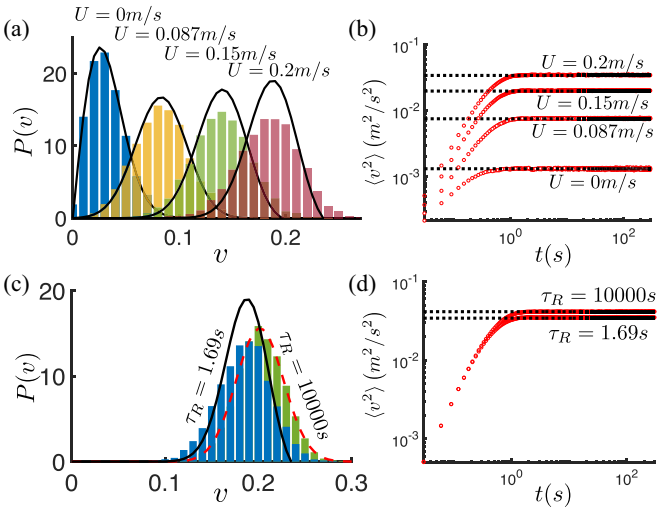

FIG. 8. (a) Theoretical and numerical comparison for an active system with parameters (taken from available experiments): $M = 1.57 \times 10^{-3}$ kg, $\tau_M = 0.33$ s, $D_T = 2.2 \times 10^{-4}$ m^2 s^{-1}, $\tau_R = 1.69$ s, and proposed propulsion speeds $U = [0, 0.087, 0.15, 0.2]$ m/s. The theoretical expression, Eq. (51), is represented as a solid black line. (b) MSS for the active system in panel (a), where red points represent the numerical results and the dashed black lines represent the theoretical expression, Eq. (64). (c) Active system with parameters (taken from previous experiments): $M = 1.57 \times 10^{-3}$ kg, $\tau_M = 0.33$ s, $D_T = 2.2 \times 10^{-4}$ m^2 s^{-1}, $U = 0.2$ m/s, and with $\tau_R = [10000, 1.69]$ s. Here, Eq. (51) is represented, respectively, in black-solid and red-dashed lines. Notice how the maxima of the distributions move to the right-hand side when $\tau_R \to \infty$. (d) MSS for the system in panel (c).

taken into account. The number of eigenvalues used to plot the analytical distribution, Eq. (51) (black solid lines), were $N = 25$. A good agreement between theory and simulations can be observed. However, as the propulsion speed U increases, the maximum values for $P_v(v)$, according to the theory and the simulations, do not perfectly match. To overcome this observation, higher orders in the perturbation series would have to be included. The effect of the rotational diffusion on the steady speed distribution is also visualized in Fig. 8(c). Here, in addition to the use of the same parameters as in Sec. IV, a propulsion speed $U = 0.2$ m/s, and two different rotational diffusivities, $\tau_R = [10000, 1.69]$ s, are considered. Notice how $\tau_R = 10\,000$ s represents the perfect bimodal case $\tau_R \to \infty$. It can be seen that as τ_R reduces, the speed distribution is displaced to the left. This just means that a small τ_R does not allow the particle to maintain its net velocity close to its propulsion speed. Notice that the analytical, Eq. (51), is plotted as black solid and red dashed lines, respectively. It can also be seen that, as τ_R increases, the analytical solution fits better to the simulation. Therefore, for smaller τ_R, while fixing τ_M, higher orders in the perturbation series would be needed to observe a better match between theory and simulations.

D. Mean square speed in two dimensions

To close this work, let us evaluate the system's mean square speed. Due to isotropy, one can calculate it using that $\langle v_j^2 \rangle = \int_{-\infty}^{\infty} v_j^2 P(v_j) dv_j$ together with $\langle v^2 \rangle = 2\langle v_j^2 \rangle$ for $j = \{x, y\}$. It is worth noticing that, by using numerical integration to calculate the angular marginal to Eq. (47), it is possible to verify that $P(v_x) = P(v_y)$ as expected. Thus by simply using the result given by Eq. (40), one gets

$$\langle v^2 \rangle = 2\left[\frac{D_T}{\tau_M} + \frac{U^2}{2}\left(1 - \frac{\tau_M}{\tau_R}\right)\right]. \tag{64}$$

Its plot can be seen in Figs. 8(b) and 8(d), where the MSS for the systems considered in Figs. 8(a) and 8(c) are calculated. In this figure, black dashed lines represent the theoretical expression, Eq. (64), whereas red dotted lines represent the numerical results. Notice the excellent agreement between theory and simulations.

IX. CONCLUSIONS

This work was able to extract—after using the periodicity of the active term, a Fourier transform, and so on—the core structure of the active Fokker-Planck equation [Eq. (6)]. By using that structure, this paper solved the steady FP equation using perturbation methods and analytically revealed the condition under which a noninteractive active system presents either a bimodal or a Gaussian velocity distribution. This condition was shown to depend on the reorientation and translational inertial timescales in active matter. When the inertial time is smaller than the orientation time, the active Fokker-Planck stationary solution admits a bimodal shape. The inverse condition was shown to admit a Gaussian shape. The treatment in this work of an active system with a large inertial relaxation time closes the gap in the current literature, where only the small-mass limit (equivalent to a high dissipation condition or to a small inertial relaxation time) was considered. The latter procedure was carried out in one and two dimensions; in particular, in a two-dimensional (2D) environment and for a system with its inertial time smaller than its orientation time, a volcano-like shape for the velocity profile was obtained. Its respective speed distribution was also analytically found thanks to a spotted mathematical identity for the first-kind Bessel function as a sum of bimodal exponential functions. Interestingly, this speed distribution was seen to be very close to a Gaussian distribution. Once the mentioned velocity distributions were available, the mean square speed (MSS) for the system was also extracted. It was observed that active matter with a Gaussian velocity distribution presents a smaller MSS than a system with a bimodal velocity distribution. The latter result may have important effects in collective animal behavior where information transfer may depend on the members' speed. Langevin dynamics simulations—in one and two dimensions—were also performed and their comparison with the analytical results showed an excellent agreement, thus validating the analytical findings in this work.

ACKNOWLEDGMENTS

M.S. and P.H. recognize the support of this research through the National Council of Humanities, Science, and Technology (CONAHCYT) mechanism.

TABLE I. Eigenvalues of matrix $\mathbb{A}$ for different N.

N	3	5	7	9	15
w_1	2	2	2	2	2
w_2	$2+\sqrt{3}$	3.176	3.950	3.9696	3.9890
w_3	$2-\sqrt{3}$	0.824	0.050	3.7321	3.9021
w_4		3.902	2.868	3.2856	3.7321
w_5		0.098	1.132	2.6840	3.4863
w_6			3.564	0.0304	3.1756
w_7			0.436	0.2679	2.8135
w_8				1.3160	2.4158
w_9				0.7144	1.5842
w_{10}					0.0110
w_{11}					0.0979
w_{12}					0.2679
w_{13}					0.5137
w_{14}					1.1865
w_{15}					0.8244

APPENDIX A: EIGENVALUES PROPERTIES

This Appendix deals with some important properties from matrix $\mathbb{A}$ (size $2N \times 2N$). Those properties together with numerical analysis helped us to formulate a theoretical expression for its respective eigenvalues, as described below. First, some of its eigenvalues—for different values of N—can be visualized in Table I. Thus, one can notice that matrix $\mathbb{A}$ has N different eigenvalues, which implies that each eigenvalue w_i has a multiplicity of two. The characteristic polynomial associated with $\mathbb{A}$, has the factorized form

$$P(\lambda) = (\lambda - w_1)^2(\lambda - w_2)^2(\lambda - w_3)^2 \cdots (\lambda - w_N)^2. \quad \text{(A1)}$$

However, to obtain a general analytical expression for w_i from Eq. (A1) is impossible. Instead, we employed numerical analysis to obtain the eigenvalues of $\mathbb{A}$ for different N and deduce some of its eigenvalues properties:

(1) There exist eigenvalues w_i different than zero only for N being an odd number.

(2) For any odd N, there exists one eigenvalue with the value two. The rest of the eigenvalues change their numerical value with N.

(3) There exists an even number of different eigenvalues $N-1$. These eigenvalues can be separated into $(N-1)/2$ pairs with the property $w_i + w_j = 4$, where $w_i = 2 + k_i$ and $w_j = 2 - k_i$.

The latter observations lead to the conclusion that, for any $k \in \mathbb{Z}$,

$$\sum_{j=1}^{N} w_j^k = \frac{(2k)!N}{(k!)^2}, \quad \text{(A2)}$$

which is a very useful expression that allows us to represent analytical results in a closed form.

APPENDIX B: FIRST-KIND BESSEL FUNCTION $J_0(x)$

This Appendix formally proves the mathematical identity given by Eq. (28). First, rewrite Eq. (28) from the text as

$$J_0(x) = \frac{1}{N}\sum_{j=1}^{N} \cos\left[\frac{x\sqrt{w_j}}{2}\right]. \quad \text{(B1)}$$

Then, by using the series expansion of $\cos(x)$ and the eigenvalues property, Eq. (39), one can proceed as follows:

$$\begin{aligned}
\frac{1}{N}\sum_{j=1}^{N} \cos\left[\frac{x\sqrt{w_j}}{2}\right] &= \frac{1}{N}\sum_{j=1}^{N}\sum_{k=0}^{\infty} \frac{(-1)^k}{(2k)!}\left(\frac{x}{2}\right)^{2k} w_j^k \\
&= \frac{1}{N}\sum_{k=0}^{\infty} \frac{(-1)^k}{(2k)!}\left(\frac{x}{2}\right)^{2k} \sum_{j=1}^{N} w_j^k \\
&= \frac{1}{N}\sum_{k=0}^{\infty} \frac{(-1)^k}{(2k)!}\left(\frac{x}{2}\right)^{2k} \frac{(2k)!N}{(k!)^2} \\
&= \sum_{k=0}^{\infty} \frac{(-1)^k}{(k!)^2}\left(\frac{x}{2}\right)^{2k}, \\
&= J_0(x), \quad \text{(B2)}
\end{aligned}$$

which ends the proof. ■

[1] M. Joyeux and E. Bertin, Phys. Rev. E **93**, 032605 (2016).
[2] S. C. Takatori and J. F. Brady, Phys. Rev. Fluids **2**, 094305 (2017).
[3] O. Dauchot and V. Démery, Phys. Rev. Lett. **122**, 068002 (2019).
[4] Y. Fily, Y. Kafri, A. P. Solon, J. Tailleur, and A. Turner, J. Phys. A: Math. Theor. **51**, 044003 (2018).
[5] H. Löwen, Phys. Rev. E **99**, 062608 (2019).
[6] X. Yang and M. C. Marchetti, Phys. Rev. Lett. **115**, 258101 (2015).
[7] C. Scholz, S. Jahanshahi, A. Ldov, and H. Lowen, Nat. Commun. **9**, 1 (2018).
[8] M. Sandoval and J. F. Brady, in *APS March Meeting Abstracts*, APS Meeting (Bulletin of the American Physical Society, 2019), Abstract No. H61.00004.
[9] M. Sandoval, Phys. Rev. E **101**, 012606 (2020).
[10] J. M. Epstein, K. Klymko, and K. K. Mandadapu, J. Chem. Phys. **150**, 164111 (2019).
[11] S. Mandal, B. Liebchen, and H. Löwen, Phys. Rev. Lett. **123**, 228001 (2019).
[12] H. Löwen, J. Chem. Phys. **152**, 040901 (2020).
[13] L. L. Gutierrez-Martinez and M. Sandoval, J. Chem. Phys. **153**, 044906 (2020).
[14] A. R. Sprenger, S. Jahanshahi, A. V. Ivlev, and H. Löwen, Phys. Rev. E **103**, 042601 (2021).
[15] M. Sandoval, Soft Matter **19**, 6287 (2023).
[16] A. Cavagna, L. D. Castello, I. Giardina, T. Grigera, A. Jelic, S. Melillo, T. Mora, L. Parisi, E. Silvestri, M. Viale, and A. M. Walczak, J. Stat. Phys. **158**, 601 (2015).
[17] A. Baskaran and M. C. Marchetti, Phys. Rev. Lett. **101**, 268101 (2008).

[18] A. Baskaran and M. C. Marchetti, J. Stat. Mech.: Theory Exp. **2010**, P04019 (2010).
[19] M. Enculescu and H. Stark, Phys. Rev. Lett. **107**, 058301 (2011).
[20] S. Steffenoni, G. Falasco, and K. Kroy, Phys. Rev. E **95**, 052142 (2017).
[21] H. D. Vuijk, J. U. Sommer, H. Merlitz, J. M. Brader, and A. Sharma, Phys. Rev. Res. **2**, 013320 (2020).
[22] P. Herrera and M. Sandoval, Phys. Rev. E **103**, 012601 (2021).
[23] A. K. Omar, K. Klymko, T. GrandPre, P. L. Geissler, and J. F. Brady, J. Chem. Phys. **158**, 074904 (2023).
[24] M. Feng and Z. Hou, J. Chem. Phys. **158**, 024102 (2023).
[25] L. Caprini and U. M. B. Marconi, J. Chem. Phys. **153**, 184901 (2020).
[26] B. ten Hagen, S. van Teeffelen, and H. Loŝwen, Condens. Matter Phys. **12**, 725 (2009).
[27] P. Herrera, L. Apaza, and M. Sandoval, Mol. Phys. **118**, e1711974 (2020).
[28] N. Graznbech-Jensen and O. Farago, Mol. Phys. **111**, 983 (2013).
[29] M. Abramowitz and I. A. Stegun, *Handbook of Mathematical Functions with Formulas, Graphs, and Mathematical Tables*, Ninth Dover printing, Tenth GPO printing (Dover, New York, 1964).